Chapter 5

Measurements of the Electron Magnetic Moment

G. Gabrielse

Department of Physics, Harvard University
17 Oxford Street, Cambridge, MA 02138

New measurements determine the electron magnetic moment in Bohr magnetons, $g/2 = 1.001\,159\,652\,180\,73\,(28)\,[0.28\,\text{ppt}]$. The uncertainty is 15 times smaller than for the measurement that had stood for 20 years, and the value is shifted by 1.7 standard deviations. The cyclotron and spin states of a single trapped electron are fully resolved thanks to a cylindrical Penning trap cavity at 100 mK, cavity-modified radiation fields, inhibited spontaneous emission, and a one-particle self-excited oscillator. The new $g/2$ and QED theory determine the fine structure constant, $\alpha^{-1} = 137.035\,999\,084\,(51)\,[0.37\,\text{ppb}]$, more than an order of magnitude more accurately than any independent determination.

Contents

G. Gabrielse

Measurements of the Electron Magnetic Moment
Chapter 5 in "Lepton Moments"

Edited by Roberts and Marciano
(World Scientific, Singapore, 2010)

158   *G. Gabrielse*

5.1. Introduction and Overview

Measurements of the electron magnetic moment (μ) probe the electron's interaction with the fluctuating vacuum described by quantum electrodynamics (QED). They also probe for possible electron substructure that is not part of the Standard Model of particle physics. As an eigenstate of spin **S**, the electron (charge $-e$ and mass m) has $\mu \propto \mathbf{S}$,

$$\mu = -\frac{g}{2} \frac{e\hbar}{2m} \frac{\mathbf{S}}{\hbar/2}. \tag{5.1}$$

The g-value is a dimensionless measure of the moment, with the dimensions and approximate size given by the Bohr magneton, $e\hbar/(2m)$. Thus $g/2$ is the magnetic moment in units of Bohr magnetons for a spin 1/2 particle like an electron or muon.

If the electron was a mechanical system, and spin was an orbital angular momentum, then g would characterize the relative distributions of the rotating charge and mass, with $g = 1$ for identical distributions. (Cyclotron motion of a charge in a magnetic field B, at frequency $\nu_c = eB/(2\pi m)$, is one example.) A Dirac point particle has $g = 2$, the leading term in

$$g/2 = 1 + a_{QED}(\alpha) + a_{hadronic} + a_{weak} + a_{new}. \tag{5.2}$$

QED predicts that vacuum fluctuations and polarization slightly increase this value by the small "anomaly" $a_{QED}(\alpha) \approx 10^{-3}$ that is a function of the fine structure constant α. Hadronic and weak interactions are calculated within the Standard Model to be very small and negligible, respectively. Electron substructure (or other deviations from the Standard Model) would make $g/2$ deviate by a_{new} from the Dirac/QED prediction, as quark-gluon substructure does for a proton.

Why measure the electron $g/2$? The motivations include:

(1) The electron $g/2$ is the property that can be most accurately measured for an important ingredient of our universe, an unusual particle that is predicted to have no internal structure.

(2) The most stringent test of QED comes from measuring $g/2$ and comparing to the value $g(\alpha)$ calculated using an independently determined α in Eq. (5.2).

(3) The most accurate determination of the fine structure constant, by more than an order of magnitude, comes from solving Eq. (5.2) for α in terms of the measured $g/2$. (No physics beyond the Standard Model, i.e. $a_{new} = 0$, is assumed.)

(4) A search for physics beyond the Standard Model (e.g. electron substructure) comes from using the best measurement of $g/2$ and the best independent α (with calculated values of $a_{hadronic}$ and a_{weak}) in Eq. (5.2) to set a limit on a_{new}.

(5) Comparing $g/2$ for an electron and a positron is the most stringent test of CPT invariance with leptons.

Owing to the great importance of the dimensionless magnetic moment, there have been many measurements of the electron $g/2$. A long list of measurements of this fundamental quantity has been compiled [1]. Worthy of special mention is a long series of measurements at the Univ. of Michigan [2]. The spin precession relative to the cyclotron rotation of keV electrons was measured. Also worthy of special mention is the series of measurements at the Univ. of Washington [3]. In the end these measurements [4] used a single electron trapped in a hyperbolic Penning trap.

New Harvard measurements determine the electron magnetic moment [5, 7] to a much higher accuracy than do previous measurements. The most recent in the long history of applying new methods to measuring $g/2$, they supersede the UW measurement that stood for about 20 years [4]. The uncertainty is 15 times lower and the measured value is shifted by 1.7 standard deviations (Fig. 5.1).
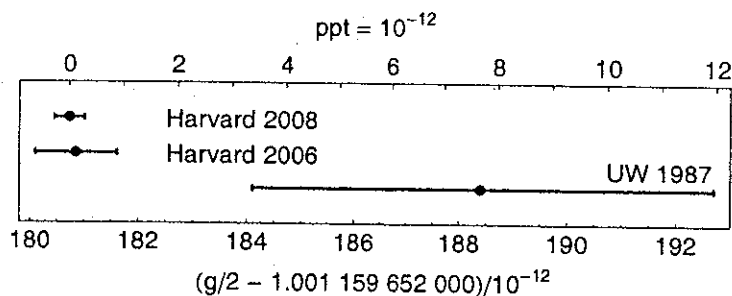

Fig. 5.1.   Most accurate measurements of the electron $g/2$.

G. Gabrielse

The substantially higher accuracy of the new measurements was the result of new experimental methods, developed and demonstrated one thesis at a time over 20 years by a string of excellent Ph.D. students – C. H. Tseng, D. Enzer, J. Tan, S. Peil, B. D'Urso, B. Odom and D. Hanneke. Progress continues in the ongoing work of Ph.D. students S. Fogwell and J. C. Dorr. The unifying idea for the new methods was that of a one-electron quantum cyclotron – with fully resolved cyclotron and spin energy levels, and a detection sensitivity sufficient to detect one quantum transitions. The new methods included:

(1) A cylindrical Penning trap was used to suspend the electron. The cylindrical trap was invented to form a microwave cavity that could inhibit spontaneous emission. The calculable cavity shape made it possible to understand and correct for cavity shifts of the measured cyclotron frequency.

(2) Cavity-inhibited spontaneous emission (by a factor of up to 250) narrowed measured linewidths and gave us the crucial averaging time that we needed to resolve one-quantum changes in the electron's cyclotron state.

(3) The cavity was cooled to 100 mK rather than to 4.2 K so that in thermal equilibrium the electron's cyclotron motion would be in its ground state.

(4) Detection with good signal-to-noise ratio came from feeding back a signal derived from the electron's motion along the magnetic field to the electron to cancel the damping due to the detection impedance. The "classical measurement system" for the quantum cyclotron motion was this large self-excited motion of the electron, with a quantum nondemolition coupling between the classical and quantum systems.

(5) A silver trap cavity avoided the magnetic field variations due to temperature fluctuations of the paramagnetism of conventional copper trap electrodes.

(6) The measurement was entirely automated so that the best data could be taken at night, when the electrical, magnetic and mechanical disturbances were lowest, with no person present.

(7) A parametric excitation of electrons suspended in the trap was used to measure the radiation modes of the radiation field in the trap cavity.

(8) The damping rate of a single trapped electron was used as a second probe of the radiation fields within the trap cavity.

5.2. One-Electron Quantum Cyclotron

5.2.1. *A homemade atom*

A one-electron quantum cyclotron is a single electron suspended within a magnetic field, with the quantum structure in its cyclotron motion fully resolved. Accurate measurements of the resonant frequencies of driven transitions between the energy levels of this homemade atom – an electron bound to our trap – reveals the electron magnetic moment in units of Bohr magnetons, $g/2$. The energy levels and what must be measured to determine $g/2$ are presented in this section. The experimental devices and methods needed to realize the one-electron quantum cyclotron are discussed in following sections.

A nonrelativistic electron in a magnetic field has energy levels

$$E(n, m_s) = \tfrac{g}{2}h\nu_c m_s + (n + \tfrac{1}{2})h\nu_c. \tag{5.3}$$

These depend in a familiar way upon the electron's cyclotron frequency ν_c and its spin frequency $\nu_s \equiv (g/2)\nu_c$. The electron $g/2$ is thus specified by the two frequencies,

$$\frac{g}{2} = \frac{\nu_s}{\nu_c} = 1 + \frac{\nu_s - \nu_c}{\nu_c} = 1 + \frac{\nu_a}{\nu_c}, \tag{5.4}$$

or equivalently by their difference (the anomaly frequency $\nu_a \equiv \nu_s - \nu_c$) and ν_c. Because ν_s and ν_c differ by only a part-per-thousand, measuring ν_a and ν_c to a precision of 1 part in 10^{10} gives $g/2$ to 1 part in 10^{13}.

Although one electron suspended in a magnetic field will not remain in one place long enough for a measurement, two features of determining $g/2$ by measuring ν_a and ν_c are apparent in Eq. (5.4).

(1) Nothing in physics can be measured more accurately than a frequency (the art of timekeeping being so highly developed) except for a ratio of frequencies.

(2) Although both of these frequencies depend upon the magnetic field, the field dependence drops out of the ratio. The magnetic field thus needs to be stable only on the time scale on which both frequencies can be measured, and no absolute calibration of the magnetic field is required.

G. Gabrielse

Measurements of the Electron Magnetic Moment
Chapter 5 in "Lepton Moments"

Edited by Roberts and Marciano
(World Scientific, Singapore, 2010)

162   *G. Gabrielse*

To confine the electron for precise measurements, an ideal Penning trap includes an electrostatic quadrupole potential $V \sim z^2 - \frac{1}{2}\rho^2$ with a magnetic field $B\hat{z}$ [7]. This potential shifts the cyclotron frequency from the free-space value ν_c to $\bar{\nu}_c$. The latter frequency is also slightly shifted by the unavoidable leading imperfections of a real laboratory trap – a misalignment of the symmetry axis of the electrostatic quadrupole and the magnetic field, and quadratic distortions of the electrostatic potential.

The lowest cyclotron energy levels (with quantum numbers $n = 0, 1, \ldots$) and the spin energy levels (with quantum numbers $m_s = \pm 1/2$) are given by

$$E(n, m_s) = \frac{g}{2}h\nu_c m_s + (n + \tfrac{1}{2})h\bar{\nu}_c - \tfrac{1}{2}h\delta(n + \tfrac{1}{2} + m_s)^2. \qquad (5.5)$$

The lowest cyclotron and spin energy levels are represented in Fig. 5.2.
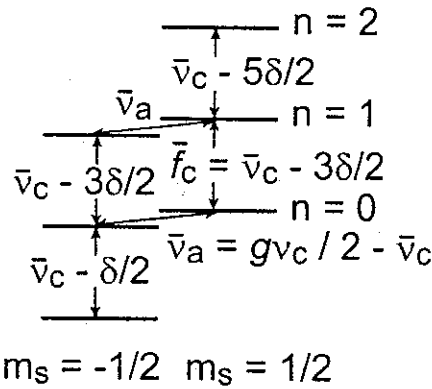

Fig. 5.2.   Lowest cyclotron and spin levels of an electron in a Penning trap.

Special relativity is important for even the lowest quantum levels. The third term in Eq. (5.5) is the leading relativistic correction [7] to the energy levels. Special relativity makes the transition frequency between two cyclotron levels $|n, m_s\rangle \leftrightarrow |n + 1, m_s\rangle$ decrease from $\bar{\nu}_c$ to $\bar{\nu}_c + \Delta\bar{\nu}_c$, with the shift

$$\Delta\bar{\nu}_c = -\delta(n + 1 + m_s) \qquad (5.6)$$

depending upon the spin state and cyclotron state. This very small shift, with

$$\delta/\nu_c \equiv h\nu_c/(mc^2) \approx 10^{-9}, \qquad (5.7)$$

is nonetheless significant at our precision. An important new feature of our measurement is that special relativity adds no uncertainty to our measurements. Quantum transitions between identified energy levels with a precisely known relativistic contribution to the energy levels are resolved. When only the average cyclotron frequency of an unknown distribution of cyclotron states was all that can be measured [4], figuring out the size of the relativistic frequency shift was difficult.

We have seen how $g/2$ is determined by the anomaly frequency ν_a and the free-space cyclotron frequency $\nu_c = eB/(2\pi m)$. However, neither of these frequencies is an eigenfrequency of the trapped electron. We actually measure the transition frequencies

$$\bar{f}_c \equiv \bar{\nu}_c - \frac{3}{2}\delta \tag{5.8}$$

$$\bar{\nu}_a \equiv \frac{g}{2}\nu_c - \bar{\nu}_c \tag{5.9}$$

represented by the arrows in Fig. 5.5 for an electron initially prepared in the state $|n = 0, m_s = 1/2\rangle$.

The needed $\nu_c = eB/(2\pi m)$ is deduced from the three observable eigenfrequencies of an electron bound in the trap by the Brown–Gabrielse invariance theorem [8],

$$(\nu_c)^2 = (\bar{\nu}_c)^2 + (\bar{\nu}_z)^2 + (\bar{\nu}_m)^2. \tag{5.10}$$

The three measurable eigenfrequencies on the right include the cyclotron frequency $\bar{\nu}_c$ for the quantum cyclotron motion we have been discussing. The second measurable eigenfrequency is the axial oscillation frequency $\bar{\nu}_z$ for the nearly-harmonic, classical electron motion along the direction of the magnetic field. The third measurable eigenfrequency is the magnetron oscillation frequency for the classical magnetron motion along the circular orbit for which the electric field of the trap and the motional electric field exactly cancel.

The invariance theorem applies for a perfect Penning trap, but also in the presence of the mentioned imperfection shifts of the eigenfrequencies . for an electron in a trap. This theorem, together with the well-defined hierarchy of trap eigenfrequencies, $\bar{\nu}_c \gg \bar{\nu}_z \gg \bar{\nu}_m \gg \delta$, yields an approximate expression that is sufficient at our accuracy. We thus determine the electron $g/2$ using

$$\frac{g}{2} = \frac{\bar{\nu}_c + \bar{\nu}_a}{\nu_c} \simeq 1 + \frac{\bar{\nu}_a - \bar{\nu}_z^2/(2\bar{f}_c)}{\bar{f}_c + 3\delta/2 + \bar{\nu}_z^2/(2\bar{f}_c)} + \frac{\Delta g_{cav}}{2}. \tag{5.11}$$

The cavity shift $\Delta g_{cav}/2$ that arises from the interaction of the cyclotron motion and the trap cavity is presently discussed in detail.

G. Gabrielse

5.2.2. *Cylindrical penning trap cavity*

A cylindrical Penning trap (Fig. 5.3) is the key device that makes these measurements possible. It was invented [9] and demonstrated [10] to provide boundary conditions that produce a controllable and understandable radiation field within the trap cavity, along with the needed electrostatic quadrupole potential. Spontaneous emission can be significantly inhibited at the same time as corresponding shifts of the electron's oscillation frequencies are avoided. We shall see that this is critical to the new Harvard measurements in several ways.
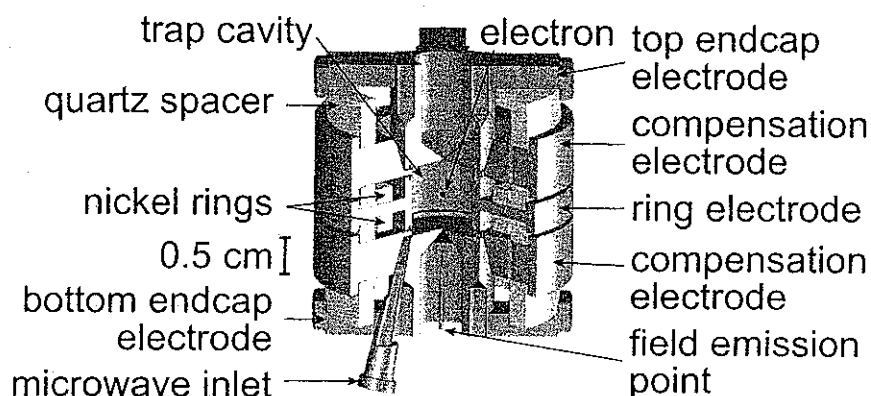

Fig. 5.3. Cylindrical Penning trap cavity used to confine a single electron and inhibit spontaneous emission.

A necessary function of the trap electrodes is to produce a very good approximation to an electrostatic quadrupole potential. This is possible with cylindrical electrodes but only if the relative geometry of the electrodes is carefully chosen [9]. The electrodes of the cylindrical trap are symmetric under rotations about the center axis ($\hat{z}$), which is parallel to the spatially uniform magnetic field ($B\hat{z}$). The potential (about 100 V) applied between the endcap electrodes and the ring electrode provides the basic trapping potential and sets the axial frequency $\bar{\nu}_z$ of the nearly harmonic oscillation of the electron parallel to the magnetic field. The potential applied to the compensation electrodes is adjusted to tune the shape of the potential, to make the oscillation as harmonic as possible. The tuning does not change $\bar{\nu}_z$ very much owing to an orthogonalization [11, 30] that arises from the geometry choice. What we found was that one electron could be observed within a cylindrical Penning trap with as good or better signal-to-noise ratio than was realized in hyperbolic Penning traps.

Table 5.1.   Properties of the trapped electron.

Cyclotron frequency	$\omega_c/(2\pi)$	150 GHz
Trap-modified cyc. freq.	$\omega_+/(2\pi)$	150 GHz
Axial frequency	$\omega_z/(2\pi)$	200 MHz
Magnetron frequency	$\omega_-/(2\pi)$	133 kHz
Cyclotron damping (free space)	τ_+	0.09 s
Axial damping	τ_z	30 ms
Magnetron damping	τ_-	10^9 yr

The principle motivation for the cylindrical Penning trap is to form a microwave cavity whose radiation properties are well understood and controlled – the best possible approximation to a perfect cylindrical trap cavity. (Our calculation attempts with a hyperbolic trap cavity were much less successful [12].) The modes of the electromagnetic radiation field that are consistent with this boundary condition are the well-known transverse electric TE_{mnp} and transverse magnetic TM_{mnp} modes (see e.g. [13, Sec. 8.7]).

For a right circular cylinder of diameter $2\rho_0$ and height $2z_0$ the TE and TM modes have characteristic resonance frequencies,

$$TE: \quad \omega_{mnp} = c\sqrt{\left(\frac{x'_{mn}}{\rho_0}\right)^2 + \left(\frac{p\pi}{2z_0}\right)^2} \tag{5.12a}$$

$$TM: \quad \omega_{mnp} = c\sqrt{\left(\frac{x_{mn}}{\rho_0}\right)^2 + \left(\frac{p\pi}{2z_0}\right)^2}. \tag{5.12b}$$

They are indexed with integers

$$m = 0, 1, 2, \cdots \tag{5.13}$$

$$n = 1, 2, 3, \cdots \tag{5.14}$$

$$p = 1, 2, 3, \cdots, \tag{5.15}$$

and are functions of the nth zeros of Bessel functions and their derivatives

$$J_m(x_{mn}) = 0 \tag{5.16}$$

$$J'_m(x'_{mn}) = 0. \tag{5.17}$$

The zeros force the boundary conditions at the cylindrical wall. All but the $m = 0$ modes are doubly degenerate.

Of primary interest is the magnitude of the cavity electric fields that couple to the cyclotron motion of an electron suspended in the center of

the trap. For both TE and TM modes, the transverse components of **E** are proportional to

$$\sin\left(\frac{p\pi}{2}\left(\frac{z}{z_0}+1\right)\right) = \begin{cases} (-1)^{p/2}\sin\left(\frac{p\pi z}{2z_0}\right) & \text{for even } p, \\ (-1)^{(p-1)/2}\cos\left(\frac{p\pi z}{2z_0}\right) & \text{for odd } p. \end{cases} \tag{5.18}$$

For an electron close to the cavity center, ($z \approx 0$), only modes with odd p thus have any appreciable coupling.

The transverse components of the electric fields are also proportional to either the order-m Bessel function times m/ρ for the TE modes, or to the derivative of the order-m Bessel function for the TM modes. Close to the cavity center ($\rho \approx 0$),

$$\frac{m}{\rho}\, J_m(x_{mn}^{(\prime)}\tfrac{\rho}{\rho_0}) \sim \begin{cases} \dfrac{\rho^{m-1}}{(m-1)!}\left(\dfrac{x_{mn}^{(\prime)}}{2\rho_0}\right)^m & \text{for } m > 0 \\ 0 & \text{for } m = 0 \end{cases} \tag{5.19a}$$

$$\frac{x_{mn}^{(\prime)}}{\rho_0} J_m'(x_{mn}^{(\prime)}\tfrac{\rho}{\rho_0}) \sim \begin{cases} \dfrac{\rho^{m-1}}{(m-1)!}\left(\dfrac{x_{mn}^{(\prime)}}{2\rho_0}\right)^m & \text{for } m > 0 \\ -\dfrac{x_{0n}^{(\prime)2}}{2\rho_0^2}\rho & \text{for } m = 0. \end{cases} \tag{5.19b}$$

In the limit $\rho \to 0$, all but the $m = 1$ modes vanish.

For a perfect cylindrical cavity the only radiation modes that couple to an electron perfectly centered in the cavity are $\text{TE}_{1n(\text{odd})}$ and $\text{TM}_{1n(\text{odd})}$. If the electron is moved slightly off-center axially it will begin to couple to radiation modes with $mnp = 1n(\text{even})$. If the electron is moved slightly off-center radially it similarly begins to couple to modes with $m \neq 1$.

In the real trap cavity, the perturbation caused by the small space between the electrodes is minimized by the use of "choke flanges" – small channels that tend to reflect the radiation leaking out of the trap back to cancel itself, and thus to minimize the losses from the trap. The measured radiation modes, discussed later, are close enough to the calculated frequencies for a perfect cylindrical cavity that we have been able to identify more than 100 different radiation modes for such trap cavities [14–16]. The spatial properties of the electric and magnetic field for the radiation that builds up within the cavity are thus quite well understood. Some of the modes couple to cyclotron motion of an electron centered in the cavity, others couple to the spin of a centered electron, and still others have the symmetry that we hope will one day allow us to sideband-cool the axial motion.

5.2.3. *100 mK and 5 T*

Detecting transitions between energy levels of the quantum cyclotron requires that the electron-bound-to-the-trap system be prepared in a definite quantum state. Two key elements are a high magnetic field, and a low temperature for the trap cavity. A high field makes the spacing of the cyclotron energy levels to be large. A high field and low temperature make a very large Boltzmann probability to be in the lowest cyclotron state, $P \propto \exp[-h\bar{\nu}_c/(kT)]$, which is negligibly different from unity.

The trap cavity is cooled to 0.1 K or below via a thermal contact with the mixing chamber of an Oxford Instruments Kelvinox 300 dilution refrigerator (Fig. 5.4). The electrodes of this trap cavity are housed within a separate vacuum enclosure that is entirely at the base temperature. Measurements on an apparatus with a similar design but at 4.2 K found the vacuum in the enclosure to be better than 5×10^{-17} torr [17]. Our much lower temperature make our background gas pressure much lower. We are able
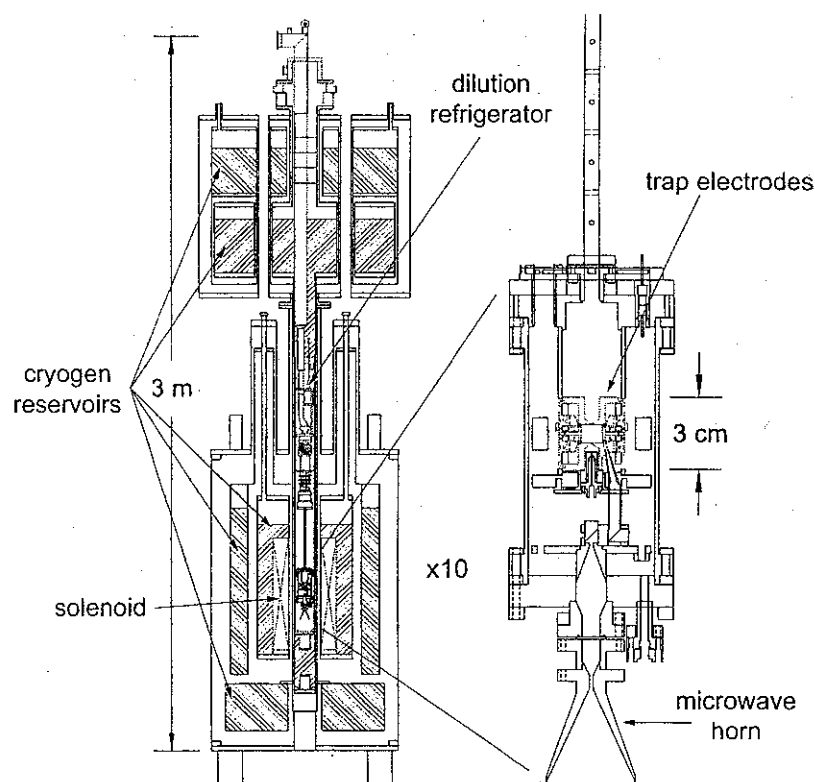

Fig. 5.4.   The apparatus includes a trap electrodes near the central axis, surrounded by a superconducting solenoid. The trap is suspended from a dilution refrigerator.

168   *G. Gabrielse*

to keep one electron suspended in our apparatus for as long as desired – regularly months at a time. Substantial reservoirs for liquid helium and liquid nitrogen make it possible to keep the trap cold for five to seven days before the disruption of adding more liquid helium or nitrogen is required.

The trap and its vacuum container is located within a superconducting solenoid (Fig. 5.4) that makes a very homogeneous magnetic field over the interior volume of the trap cavity. A large dewar sitting on top of the solenoid dewar provides the helium needed around the dilution refrigerator below. The superconducting solenoid is entirely self-contained, with a bore that can operate from room temperature down to 77 K. It possesses shim coils capable of creating a field homogeneity better than a part in 10^8 over a 1 cm diameter sphere and has a passive "shield" coil that reduces fluctuations in the ambient magnetic field [18, 19]. When properly energized (and after the steps described in the next section have been taken) it achieves field stability better than a part in 10^9 per hour. We regularly observe drifts below 10^{-9} per night.

5.2.4. *Stabilizing the energy levels*

Measuring the electron $g/2$ with a precision of parts in 10^{13} requires that the energy levels of our homemade atom, an electron bound to a Penning trap, be exceptionally stable. The energy levels depend upon the magnetic field and upon the potential that we apply to the trap electrodes. The magnetic field must be stable at least on the timescale that is required to measure the two frequencies, $\bar{f}_c$ and $\bar{\nu}_a$, that are both proportional to the magnetic field.

One defense against external field fluctuations is a high magnetic field. This makes field fluctuations due to outside sources to be relatively smaller. The largest source of ambient magnetic noise is a subway that produces 50 nT (0.5 mG, 10 ppb) fluctuations in our lab and that would limit us to four hours of data taking per day (when the subway stops running) if we did not shield the electron from them. Eddy currents in the high-conductivity aluminum and copper cylinders of the dewars and the magnet bore shield high-frequency fluctuations [20]. For slower fluctuations, the aforementioned shelf-shielding solenoid [18] has the correct geometry to make the central field always equal to the average field over the solenoid cross-section. This translates flux conservation into central-field conservation, shielding external fluctuations by more than a factor of 150 [19].

Stabilizing the field produced by the solenoid requires that care is taken when the field value is changed, since changing the current in the solenoid alters the forces between windings. Resulting stresses can take months to stabilize if the coil is not pre-stressed by "over-currenting" the magnet. Our recipe is to overshoot the target value by a few percent of the change, undershoot by a similar amount, and then move to the desired field.

The apparatus in Fig. 5.4 evolved historically rather than being designed for maximum magnetic field stability in the final configuration. Because the solenoid and the trap electrodes are suspended from widely separated support points, temperature and pressure changes can cause the electrodes to move relative to the solenoid. Apparatus vibrations can do the same insofar as the magnetic field is not perfectly homogeneous, despite careful adjusting of the persistent currents in ten superconducting shim coils. Any relative motion of the electron and solenoid changes the field seen by the electron.

To counteract this, we regulate the five He and N_2 pressures in the cryostats to maintain the temperature of both the bath and the solenoid itself [21, 22]. Recently we also relocated the dilution refrigerator vacuum pumps to an isolated room at the end of a 12 m pipe run. This reduced vibration by more than an order of magnitude at frequencies related to the pump motion and reduced the noise level for the experimenters but did not obviously improve the $g/2$ data.

Because some of the structure establishing the relative location of the trap electrodes and the solenoid is at room temperature, changes in room temperature can move the electron in the magnetic field. The lab temperature routinely cycles 1–2 K daily, so we house the apparatus in a large, insulated enclosure within which we actively regulate the air temperature to 0.1 K. A refrigerated circulating bath (ThermoNeslab RTE-17) pumps water into the regulated zone and through an automobile transmission fluid radiator, heating and cooling the water to maintain constant air temperature. Fans couple the water and air temperatures and keep a uniform air temperature throughout.

The choice of materials for the trap electrodes and its vacuum container is also crucial to attaining high field stability [5, 23]. Copper trap electrodes, for example, have a nuclear paramagnetism at 0.1 mK that makes the electron see a magnetic field that changes at an unacceptable level with very small changes in trap temperature. We thus use only low-Curie-constant materials such as silver, quartz, titanium, and molybdenum at the refrigerator base temperature and we regulate the mixing chamber temperature to 1 mK or better.

G. Gabrielse

A stable axial frequency is also extremely important since small changes in the measured axial frequency reveal one-quantum transitions of the cyclotron and spin energy (as will be discussed in Sec. 5.3.1). A trapping potential without thermal fluctuations is provided by a charged capacitor ($10\mu F$) that has a very low leakage resistance at low temperature. We add to or subtract from the charge on the capacitor using 50 ms current pulses sent to the capacitor through a 100 $M\Omega$ resistor as needed to keep the measured axial frequency constant. Because of the orthogonalized trap design [9] already discussed, the potential applied to the compensation electrodes (to make the electron see as close to a pure electrostatic quadrupole potential as possible) has little effect upon the axial frequency.

5.2.5. *Motions and damping of the suspended electron*

We load a single electron using an electron beam from a sharp tungsten field emission tip. A hole in the bottom endcap electrode admits the beam, which hits the top endcap electrode and releases gas atoms cryopumped on the surface. Collisions between the beam and gas atoms eventually cause an electron to fall into the trap. Adjusting the beam energy and the time it is on determines the number of electrons loaded.

The electron has three motions in the Penning trap formed by the $B = 5.4$ T magnetic field, and the electrostatic quadrupole potential. The cyclotron motion in the trap has a cyclotron frequency $\bar{\nu}_c \approx 150$ GHz. The axial frequency, for the harmonic oscillator parallel to the magnetic field direction, is $\bar{\nu}_z \approx 200$ MHz. A circular magnetron motion, perpendicular to **B**, has an oscillation frequency, $\bar{\nu}_m \approx 133$ kHz. The spin precession frequency, which we do not measure directly, is slightly higher than the cyclotron frequency. The frequency difference is the anomaly frequency, $\bar{\nu}_a \approx 174$ MHz, which we do measure directly.

The undamped spin motion is essentially uncoupled from its environment [7]. The cyclotron motion is only weakly damped. By controlling the cyclotron frequency relative to that of the cavity radiation modes, we alter the density of radiation states and inhibit the spontaneous emission of synchrotron radiation [7, 24] by 10 to 50 times the $(90\text{ ms})^{-1}$ free-space rate. Blackbody photons that could excite from the cyclotron ground state are eliminated because the trap cavity is cooled by the dilution refrigerator to 100 mK [25]. The axial motion is cooled by a resonant circuit at a rate $\gamma_z \approx (0.2\text{ s})^{-1}$ to as low as 230 mK (from 5 K) when the detection amplifier is off. The magnetron radius is minimized with axial sideband cooling [7].

5.3. Non-destructive Detection of One-Quantum Transitions

5.3.1. *QND detection*

Quantum nondemolition (QND) detection has the property that repeated measurements of the energy eigenstate of the quantum system do not change the state of the quantum system [26, 27]. This is crucial for detecting one-quantum transitions in the cyclotron motion insofar as it avoids transitions produced by the detection system. In this section we discuss the QND coupling, and in the next section the self-excited oscillator readout system.

Detecting a single 150 GHz photon from the decay of one cyclotron energy level to the level below would be very difficult – because the frequency is so high and because it is difficult to cover the solid angle into which the photon could be emitted. Instead we get the one-quantum sensitivity by coupling the cyclotron motion to the orthogonal axial motion at 200 MHz, a frequency at which we are able to make sensitive detection electronics [28]. The QND detection keeps the thermally driven axial motion of the electron from changing the state of the cyclotron motion.

We use a magnetic bottle gradient that is familiar from plasma physics and from earlier electron measurements [9, 29],

$$\Delta \mathbf{B} = B_2 \left[\left(z^2 - \rho^2/2 \right) \hat{\mathbf{z}} - z\rho\hat{\rho} \right], \qquad (5.20)$$

with $B_2 = 1540$ T/m^2. This is the lowest order gradient that is symmetric under reflections $z \rightarrow -z$ and is cylindrically symmetric about $\hat{z}$. The gradient arises from a pair of thin nickel rings (Fig. 5.3) that are completely saturated in the strong field from the superconducting solenoid. To lowest order the rings modify B by $\approx -0.7\%$ – merely changing the magnetic field that the electron experiences without affecting our measurement.

The formal requirement for a QND measurement is that the Hamiltonian of the quantum system (i.e. the cyclotron Hamiltonian) and the Hamiltonian describing the interaction of the quantum system and the classical measurement system must commute. The Hamiltonian that couples the quantum cyclotron and spin motions to the axial motion does so. It has the form $-\mu B$, where μ is the magnetic moment associated with the cyclotron motion or the spin. The coupling Hamiltonian thus has a term that goes as μz^2. This term has the same spatial symmetry as does the axial Hamiltonian, $H = \frac{1}{2}m(2\pi\bar{\nu}_z)^2 z^2$. A change in the magnetic moment that takes place from a one-quantum change in the cyclotron or spin magnetic·

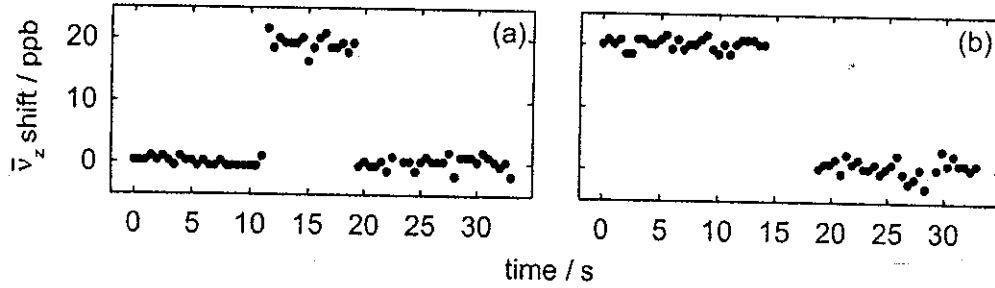172   *G. Gabrielse*

Fig. 5.5. Two quantum jumps: A cyclotron jump (a) and spin flip (b) measured via a
QND coupling to shifts in the axial frequency.

moment thus changes the observed axial frequency of the suspended electron.

The result is that the frequency of the axial motion $\bar{\nu}_z$ shifts by

$$\Delta\bar{\nu}_z = \delta_B(n + m_s), \qquad (5.21)$$

in proportion to the cyclotron quantum number n and the spin quantum number m_s. Fig. 5.5 shows the $\Delta\bar{\nu}_z = 4$ Hz shift in the 200 MHz axial frequency that takes place for one-quantum changes in cyclotron (Fig. 5.5(a)) and spin energy (Fig. 5.5(b)). The 20 ppb shift is easy to observe with an averaging time of only 0.5 s. We typically measure with an averaging time that is half this value.

5.3.2. *One-electron self-excited oscillator*

The QND coupling makes small changes in the electron's axial oscillation frequency, the signature of one-quantum cyclotron transitions and spin flips. Measuring these small frequency changes is facilitated by a large axial oscillation amplitude. To this end we use electrical feedback which we demonstrated could be used effectively to either cool the axial motion [30] or to make a large self-excited axial oscillation [31]. Cyclotron excitations and spin flips are generally induced while the detection system is off, as will be discussed. After an attempt to excite the cyclotron motion or to flip the spin has been made, the detection system is then turned on. The self-excited oscillator rapidly reaches steady state, and its oscillation frequency is then measured by fourier transforming the signal.

The 200 MHz axial frequency lies in the radio-frequency (RF) range which is more experimentally accessible than the microwave range of the 150 GHz cyclotron and spin frequencies, as mentioned. Nevertheless, standard RF techniques must be carefully tailored for our low-noise, cryogenic experiment. The electron axial oscillation induces image currents in the trap

electrodes that are proportional to the axial velocity of the electron [7, 32]. An inductor (actually the inductance of a cryogenic feedthrough) is placed in parallel with the capacitance between two trap electrodes to cancel the reactance of the capacitor which would otherwise short out the induced signal. The RF loss in the tuned circuit that is formed is an effective resistance that damps the axial motion.

The voltage that the electron motion induces across this effective resistance is amplified with two cryogenic detection amplifiers. The heart of each amplifier is a single-gate high electron mobility transistor (Fujitsu FHX13LG).

The first amplifier is at the 100 mK dilution refrigerator base temperature. Operating this amplifier without crashing the dilution refrigerator requires operating with a power dissipation in the FET that is three orders of magnitude below the transistor's 10 mW design dissipation. The effective axial temperature for the electron while current is flowing through the FET is about 5 K, well above the ambient temperature. Very careful heat sinking makes it possible for the effective axial temperature of the electron to cool to below 350 mK in several seconds after the amplifier is turned off, taking the electron axial motion to this temperature. Cyclotron excitations and spin flips are induced only when the axial motion is so cooled, with the detection amplifiers off, since the electron is then making the smallest possible excursion in the magnetic bottle gradient.

The second cryogenic amplifier is mounted on the nominally 600 mK still of the dilution refrigerator. This amplifier counteracts the attenuation of a thermally-isolating but lossy stainless steel transmission line that carries the amplified signal out of the refrigerator. The second amplifier boosts the signal above the noise floor of the first room-temperature amplifier.

Because the induced image-current signal is proportional to the electron's axial velocity, feeding this signal back to drive the electron alters the axial damping force, a force that is also proportional to the electron velocity. Changing the feedback gain thus changes the damping rate. As the gain increases, the damping rate decreases as does the effective axial temperature of the electron, in accord with the fluctuation dissipation theorem [33]. Feedback cooling of the one-electron oscillator from 5.2 K to 850 mK was demonstrated [30]. The invariant ratio of the separately measured damping rate and the effective temperature was also demonstrated, showing that the amplifier adds very little noise to the feedback.

Setting the feedback gain to make the feedback drive exactly cancel the damping in the attached circuit could sustain a large axial oscillation

G. Gabrielse

Measurements of the Electron Magnetic Moment
Chapter 5 in "Lepton Moments"

Edited by Roberts and Marciano
(World Scientific, Singapore, 2010)

174

G. Gabrielse

amplitude, in principle. However, since the gain cannot be perfectly adjusted, noise fluctuations will always drive the axial oscillation exponentially away from equilibrium. We thus stabilize the oscillation amplitude using a digital signal processor (DSP) that Fourier transforms the signal in real time, and adjusts the feedback gain to keep the signal size at a fixed value.

The one-particle self-excited oscillator is turned on after an attempt has been made to excite the cyclotron energy up one level, or to flip the spin. The frequency of the axial oscillation that rapidly stabilizes at a large and easily detected amplitude is then measured. Small shifts in this frequency reveal whether the cyclotron motion has been excited by one quantum or whether the spin has flipped, as illustrated in Fig. 5.5.

5.3.3. *Inhibited spontaneous emission*

The spontaneous emission of synchrotron radiation in free space would make the damping time for an electron's cyclotron motion to be less than 0.1 s. This is not enough time to average down the noise in our detection system to the level that would allow the resolution of one-quantum transitions between cyclotron states. Also, to drive cyclotron transitions "in the dark", with the detection system off, requires that the cyclotron excitations persist long enough for the detection electronics to be turned on. Cavity-inhibition of the spontaneous emission gives us the averaging time that we need.

One of the early papers in what has come to be known as cavity QED was an observation of inhibited spontaneous emission within a Penning trap [24] – the first time that inhibited spontaneous emission was observed within a cavity and with only one particle – as anticipated earlier [34, 35]. As already mentioned, the cylindrical Penning trap [9] was invented to provide understandable boundary conditions to control the spontaneous emission rate with only predictable cavity shifts of the electron's cyclotron frequency.

The spontaneous emission rate is measured directly, by making a histogram of the time the electron spends in the first excited state after being excited by a microwave drive injected into the trap cavity with the detector left on. Fig. 5.6 shows a sample histogram which fits well to an exponential (solid curve) with a lifetime of 0.41 s in this example.

Stimulated emission is avoided by making these observations only when the cavity is at low temperature so that effectively no blackbody photons are present. The detector makes thermal fluctuations of the axial oscillation
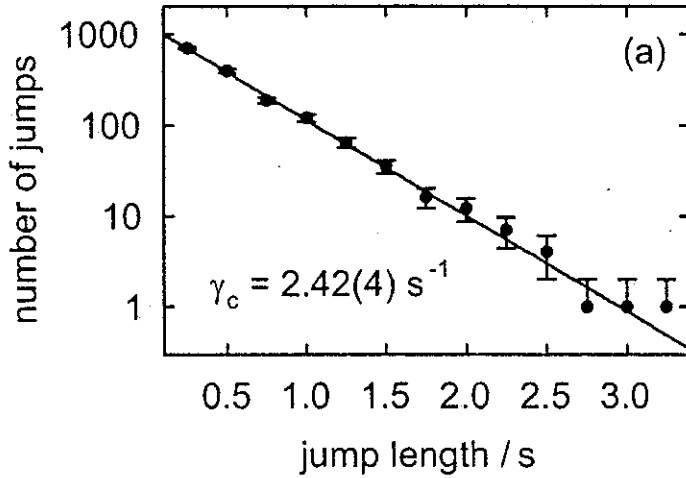
Fig. 5.6. A histogram of the time that the electron spends in the first excited state that is fit to an exponential reveals the substantial inhibition of the spontaneous emission of synchrotron radiation. The decay time, 0.41 s in this example, depends on how close the cyclotron frequency is to neighboring radiation modes of the trap cavity. Lifetimes as long as 16 s have been observed.

amplitude, and these in turn make the cyclotron frequency fluctuate. For measuring the cyclotron decay time, however, this does not matter as long as the fluctuations in axial amplitude are small compared to the 2 mm wavelength of the radiation that excites the cyclotron motion.

- The spontaneous emission rate into free space is [7]

$$\gamma_+ = \frac{4}{3}\frac{r_e}{c}(\omega_c)^2 \approx \frac{1}{0.89 \text{ ms}} \, . \tag{5.22}$$

The measured rate in this example is thus suppressed by a factor of 4.5. The density of states within the cylindrical trap cavity is not that of free space. Instead the density of states for the radiation is peaked at the resonance frequencies of the radiation modes of the cavity, and falls to very low values between the radiation modes. We attain the inhibited spontaneous emission by tuning the magnetic field so that the cyclotron frequency is as far as possible from resonance with the cavity radiation modes. With the right choice of magnetic field we have increased the lifetime to 16 s, which is a cavity suppression of spontaneous emission by a factor of 180.

In a following section we report on using the direct measurements of the radiation rate for electron cyclotron motion to probe the radiation modes of the cavity, with the radiation rate increasing sharply at frequencies that approach a resonant mode of the cavity.

176   *G. Gabrielse*

5.4. Elements of an Electron $g/2$ Measurement

5.4.1. *Quantum jump spectroscopy*

We determine the cyclotron and anomaly frequencies using quantum jump spectroscopy, in which a near resonance drive attempts to either excite the cyclotron motion or flip the spin. After each attempt we check whether a one-quantum transition has taken place, and build up a histogram of transitions per attempt. Fig. 5.7 shows the observed quantum jump lineshapes upon which our 2008 measurement is based.

A typical data run consists of alternating scans of the cyclotron and anomaly lines. The runs occur at night, with daytime runs only possible on Sundays and holidays when the ambient magnetic field noise is lower. Interleaved every three hours among these scans are periods of magnetic field monitoring to track long-term drifts using the electron itself as the magnetometer. In addition, we continuously monitor over fifty environmental parameters such as refrigerator temperatures, cryogen pressures and flows, and the ambient magnetic field in the lab so that we may screen data for abnormal conditions and troubleshoot problems.

Cyclotron transitions are driven by injecting microwaves into the trap cavity. The microwaves originate as a 15 GHz drive from a signal generator (Agilent E8251A) whose low-phase-noise, 10 MHz oven-controlled crystal oscillator serves as the timebase for all frequencies in the experiment. After passing through a waveguide that removes all subharmonics, the signal enters a microwave circuit that includes an impact ionization avalanche transit-time (IMPATT) diode, which multiplies the frequency by ten and outputs the $\bar{f}_c$ drive at a power of 2 mW. Voltage-controlled attenuators reduce the strength of the drive, which is broadcast from a room temperature horn through teflon lenses to a horn at 100 mK (Fig. 5.4) and enters the trap cavity through an inlet waveguide (Fig. 5.3).

Anomaly transitions are driven by potentials, oscillating near $\bar{\nu}_a$, applied to electrodes to drive off-resonant axial motion through the magnetic bottle gradient (Eq. (5.20)). The gradient's $z\rho\hat{\rho}$ term mixes the driven oscillation of z at $\bar{\nu}_a$ with that of ρ at $\bar{f}_c$ to produce an oscillating magnetic field perpendicular to B as needed to flip the spin. The axial amplitude required to produce the desired transition probability is too small to affect the lineshape (Sec. 5.4.4); nevertheless, we apply a detuned drive of the same strength during cyclotron attempts so the electron samples the same magnetic gradient.

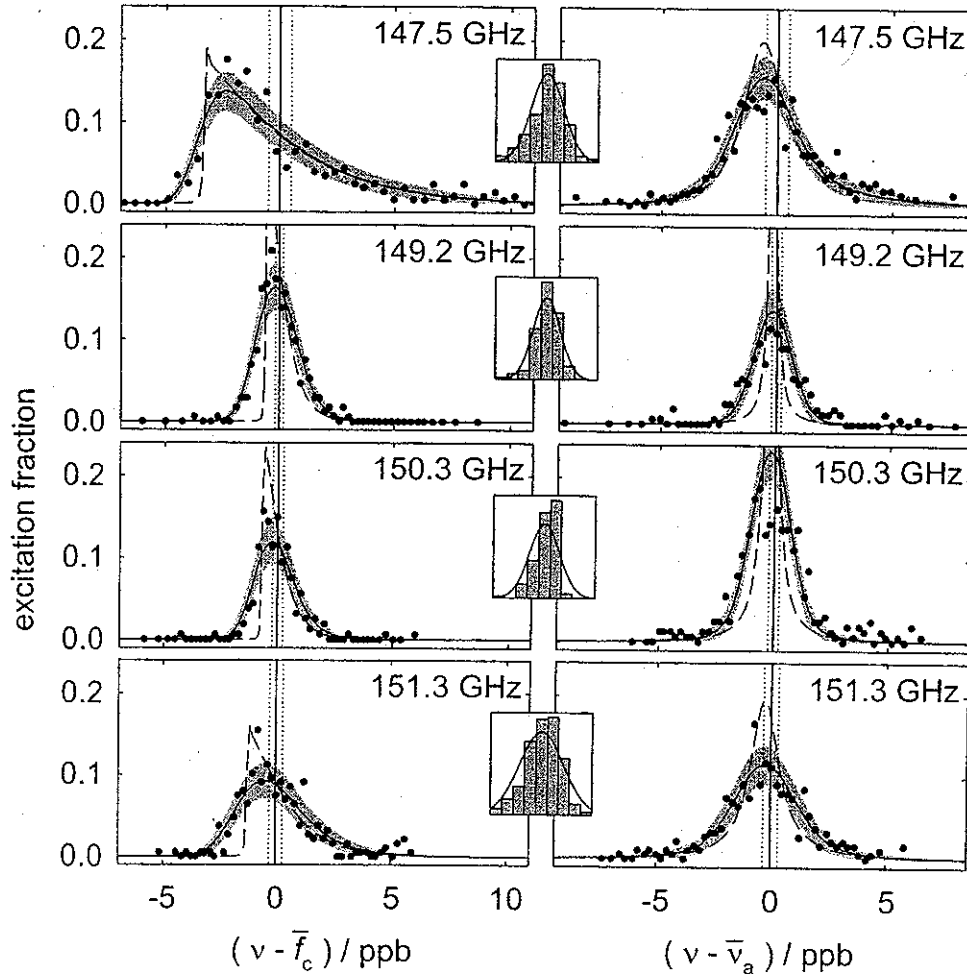*Measurements of the Electron Magnetic Moment*   177

Fig. 5.7. Quantum-jump spectroscopy lineshapes for cyclotron (left) and anomaly (right) transitions with maximum-likelihood fits to broadened lineshape models (solid) and inset resolution functions (solid) and edge-tracking data (histogram). Vertical lines show the 1-σ uncertainties for extracted resonance frequencies. Corresponding unbroadened lineshapes are dashed. Gray bands indicate 1-σ confidence limits for distributions about broadened fits. All plots share the same relative frequency scale.

Quantum jump spectroscopy of each resonance follows the same procedure. With the electron prepared in the spin-up ground state $|0, \frac{1}{2}\rangle$, the magnetron radius is reduced with 1.5 s of strong sideband cooling at $\bar{\nu}_z + \bar{\nu}_m$ with the SEO turned off immediately and the detection amplifiers turned off after 0.5 s. After an additional 1 s to allow the axial motion to thermalize with the tuned circuit, we apply a 2 s pulse of either a cyclotron drive near $\tilde{f}_c$ or an anomaly drive near $\bar{\nu}_a$ with the other drive applied simultaneously but detuned far from resonance. The detection electronics and SEO are

178   *G. Gabrielse*

turned back on; after waiting 1 s to build a steady-state axial amplitude, we measure $\bar{\nu}_z$ and look for a 20 ppb shift up (from a cyclotron transition) or down (from an anomaly transition followed by a spontaneous decay to $|0, -\frac{1}{2}\rangle$) in frequency. Cavity-inhibited spontaneous emission provides the time needed to observe cyclotron transitions before decay. The several-cyclotron-lifetimes wait for a spontaneous decay after an anomaly attempt is the rate-limiting step in the spectroscopy. After a successful anomaly transition and decay, simultaneous cyclotron and anomaly drives pump the electron back to $|0, \frac{1}{2}\rangle$. All timing is done in hardware. We probe each resonance line with discrete excitation attempts spaced in frequency by approximately 10% of the linewidth. We step through each drive frequency on the $\bar{f}_c$ line, then each on the $\bar{\nu}_a$ line, and repeat.

5.4.2. *The electron as magnetometer*

Slow drifts of the magnetic field are corrected using the electron itself as a magnetometer. Accounting for these drifts allows the combination of data taken over many days, giving a lineshape signal-to-noise that allows the systematic investigation of lineshape uncertainties at each field. For a half-hour at the beginning and end of a run and again every three hours throughout, we alter our cyclotron spectroscopy routine by applying a stronger drive at a frequency below $\bar{f}_c$. Using the same timing as above but a ten-times-finer frequency step, we increase the drive frequency until observing a successful transition. We then jump back 60 steps and begin again.

We model the magnetic field drift by fitting a polynomial to these "edge" points (so-called because the ideal cyclotron lineshape has a sharp low-frequency edge). Since we time-stamp every cyclotron and anomaly attempt, we use the smooth curve to remove any field drift. This edge-tracking adds a 20% overhead, but allows the use of data from nights with a larger than usual field drift, and the combination of data from different nights.

5.4.3. *Measuring the axial frequency*

In addition to $\bar{f}_c$ and $\bar{\nu}_a$, measuring $g/2$ requires a determination of the axial frequency $\bar{\nu}_z$ (Eq. (5.11)). To keep the relative uncertainty in $g/2$ from $\bar{\nu}_z$ below 0.1 ppt, we must know $\bar{\nu}_z$ to better than 50 ppb (10 Hz). This is easily accomplished. We routinely measure $\bar{\nu}_z$ when determining the cyclotron and spin states. However, the large self-excited oscillation amplitude in the slightly anharmonic axial potential typically results in a

10 ppb shift, compared to the $\bar{\nu}_z$ for the thermally-excited amplitude during the cyclotron and anomaly pulses. We cannot directly measure the axial frequency under the pulse conditions because the amplifiers are off. We come close when measuring $\bar{\nu}_z$ with the amplifiers on and all axial drives off. This thermal axial resonance appears as a dip on the amplifier noise resonance [32], and we use it as our measurement. The difference in $\bar{\nu}_z$ with the amplifiers on and off is negligible. A second shift comes from the interaction between the axial motion and the amplifier, which both damps the motion and shifts $\bar{\nu}_z$. The maximum shift of $\bar{\nu}_z$ is 1/4 of the damping rate, which at ≈ 1 ppb is negligible at our current precision. A third shift of $\bar{\nu}_z$ comes from the anomaly drive, which induces both a frequency-pulling from the off-resonant axial force and a Paul-trap shift from the change in effective trapping potential [36]; based on extrapolation from measured shifts at higher powers, we estimate these shifts combine to -1 ppb at the highest anomaly power used for the measurement—too small to affect $g/2$.

5.4.4. *Frequencies from lineshapes*

The cyclotron frequency $\bar{f}_c$ and anomaly frequency $\bar{\nu}_a$ (Fig. 5.2) must be determined from their respective quantum jump spectroscopy lineshapes (Fig. 5.7). The observed lineshapes are much broader than the natural linewidth that arises because the excited cyclotron state decays by the cavity-inhibited spontaneous emission of synchrotron radiation. The shape arises because the electron experiences a magnetic field that varies during the course of a measurement. Variations arise because of the electron's thermal axial motion within the magnetic bottle gradient, for example. Other possible variations could arise because the magnetic field for the Penning trap fluctuates in time, or because of a distribution of magnetron orbit sizes for the quantum jump trials.

Once the slow drift of the magnetic field (p. 178) has been removed, there is no reason for the electron to sample a different distribution of magnetic field values while the anomaly frequency is being measured compared to when the trap-modified cyclotron frequency is being measured. Each resonance shape converts the distribution of sampled magnetic field values into the corresponding distribution of frequency values. Dividing the quantum jump lineshapes into frequency bins, we obtain average cyclotron and anomaly frequencies by weighting the frequency of each bin by the number of quantum jumps in the bin, and use these average frequencies in Eq. (5.11).

G. Gabrielse

Using the weighted average frequencies will remove shifts to $g/2$ caused by the thermal axial motion of the electron within the magnetic bottle gradient, the largest source of the observed linewidth. The use of weighted average frequencies should also account for temporal fluctuations in the magnetic field of the Penning trap on the measurement time scale for the frequencies. If there is a distribution of magnetron radii for the quantum jump trials, the weighted average method should account for the resulting distribution of magnetic field values as well.

To verify the weighted averages method, and to assign safe uncertainties to the average frequencies that we deduce using it, we also analyze our measured lineshapes in a very different way. We start with an analytic calculation of the lineshape for thermal Brownian motion of the axial motion for a given axial temperature T_z [37]. We then fit the measured cyclotron and anomaly lineshapes (Fig. 5.7) to the ideal lineshape convolved with a Gaussian broadening function to take into account other sources of the magnetic field distribution. The analytically calculated lineshapes are the dashed curves in Fig. 5.7, the maximum-likelihood fits to the broadened lineshapes are solid curves, and the gray bands indicate where we would expect 68% of the measured points to lie. The insets to Fig. 5.7 show the best-fit resolution functions. We assign a lineshape uncertainty that is the size of the differences between the $g/2$ value determine from the fitting and our preferred weighted averages method.

The linewidths are wider for two of the four measurements in Fig. 5.7, and they remained reproducible over the weeks required to take each data point. A wider cyclotron linewidth indicates a higher axial temperature. We know of no reason why the axial temperatures should be different for different values of the Penning trap field; this is one reason that we assigned the larger uncertainties that reflect the difference between the two methods. The narrower lineshapes have better agreement between the weighted average method and the fit method, and hence the assigned lineshape uncertainties are smaller. Not surprisingly, the narrower lines better determine the corresponding frequencies.

For the 2008 measurement the lineshape uncertainty is larger than any other. Future efforts will focus upon understanding and reducing the lineshape broadening and uncertainty.

5.4.5. *Cavity shifts*

Despite the precision reached in this measurement, one correction to the directly measured $g/2$ value is required, the $\Delta g_{cav}/2$ included in Eq. (5.11).

G. Gabrielse | Measurements of the Electron Magnetic Moment
Chapter 5 in "Lepton Moments" | Edited by Roberts and Marciano
(World Scientific, Singapore, 2010)

The correction is a cavity shift correction that depends upon interaction of the electron with nearby cavity radiation modes. The trap cavity modifies the density of states of the radiation modes of free space, though not enough to significantly affect QED calculations of g [38]. Since the cavity shift correction depends upon the electron cyclotron frequency, we measure $g/2$ at four different cyclotron frequencies to make sure that the same $g/2$ is deduced when cavity shifts of different sizes are applied.

The cavity-inhibited spontaneous emission narrows the cyclotron resonance line, giving the time in the excited state that is needed to turn on the self-excited oscillator, and to average its signal long enough to determine the cyclotron state. Cavity shifts are the unfortunate downside of the cavity, arising because the cyclotron oscillator has its frequency pulled by its coupling to nearby radiation modes of the cavity.

The cylindrical Penning trap was invented to make a microwave cavity with a calculable geometry. Section 5.2.2 describes a perfect cylindrical trap cavity and the radiation fields that it can support. However, the trap is not perfectly machined, it changes its size as it cools from room temperature down to 0.1 K, and it has small slits that make it possible to bias sections to form a Penning trap.

The shape of the radiation fields near the center of the trap cavity are not greatly altered for the real cavity, but the resonant frequencies of the modes are slightly shifted. The frequency shifts are not enough to keep us from identifying most modes by comparing to calculated frequencies, but are large enough that we must measure the mode frequencies if we are to characterize the interaction of the cavity and an electron. The mode quality factors (resonant frequencies divided by energy damping rates) must also be determined. The decay of the radiation field within the cavity depends upon power dissipated by currents (induced in the electrodes and modified by the slits), and upon the loss of microwave power that escapes the trap despite the choke flanges in the slits.

We developed two methods to learn the resonant frequencies of the radiation modes of the real trap cavity:

(1) A cloud of electrons near the center of the trap is heated using a parametric driving force. The electrons cool via synchrotron radiation with a rate that is highest when their cyclotron frequency is resonant with a cavity radiation mode, and that is very small far from resonance [14–16, 39]. Fig. 5.8(a) shows the peaks in the signal from the electrons that correspond to resonance with cavity radiation modes that are labeled as described earlier.
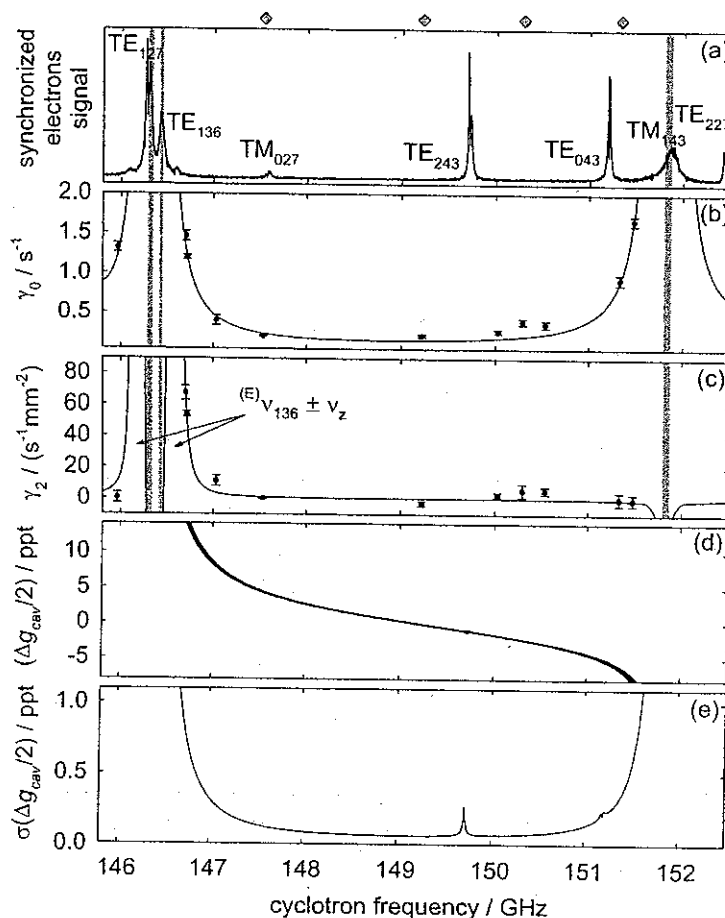
Fig. 5.8. Cavity shift results come from synchronized electrons (a) and from direct measurements with one electron of γ_c (b) and its dependence on axial amplitude (c). Together, they provide uncertainties in the frequencies of coupled cavity radiation modes (gray) that translate into an uncertainty band of cavity shifts $\Delta g_{cav}/2$ (d) whose half-width, i.e., the cavity shift uncertainty, is plotted in (e). The diamonds at the top indicate the cyclotron frequencies of the four $g/2$ measurements.

(2) The measured spontaneous emission rate for a single electron near the center of the trap cavity (Fig. 5.8b), and the dependence of this rate upon the amplitude of the axial oscillation of the electron (Fig. 5.8c), both depend upon the proximity of the electron cyclotron frequency to cavity radiation modes that couple to a nearly centered electron. Fig. 5.9 illustrates how the one-electron damping rate and dependence upon axial oscillation amplitude are measured.

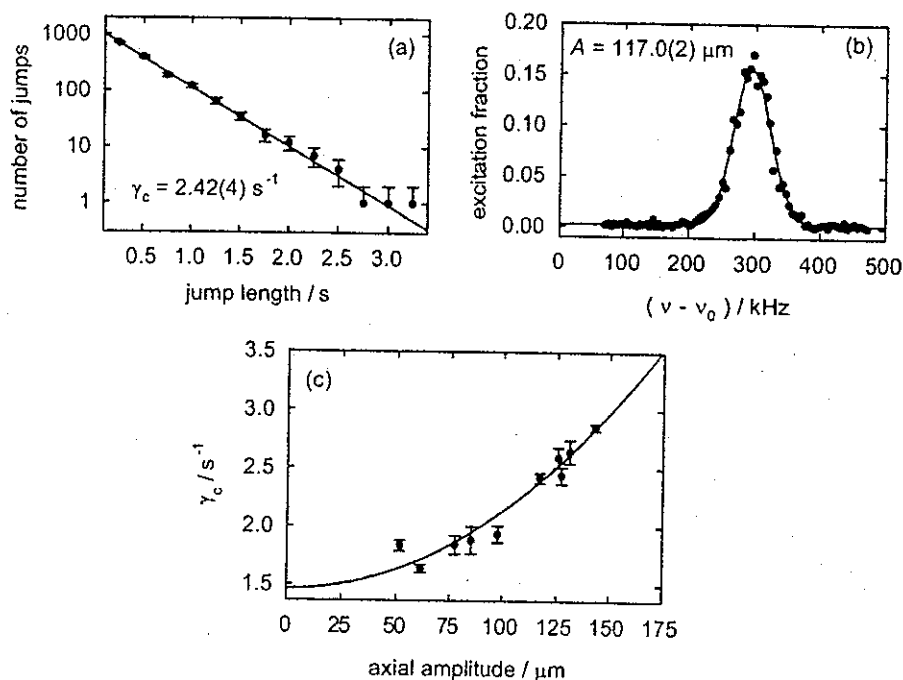*Measurements of the Electron Magnetic Moment* 183

Fig. 5.9. Measurement of the cyclotron damping rate at 146.70 GHz, near the upper sideband of TE_{136}. The cyclotron damping rate as a function of axial amplitude (c) extrapolates to the desired lifetime. Each point in (c) consists of a damping rate measured from a fit to a histogram of cyclotron jump lengths (a) as well as an axial amplitude measured from a driven cyclotron line (b).

From the cavity spectra in Figs. 5.8(a-c) we deduce the mode frequencies and uncertainties represented by the gray bands in these figures. Our identification of the modes is aided by several features of the spectra. Modes that are strongly coupled to the electrons (the coupling increases with electron number) can split into two normal modes. A large axial oscillation during measurements of the cavity spectrum produces sidebands at the axial frequency for modes with a node at the trap center, and at twice the sideband frequency for radiation modes with an antinode at the center. Modes which would not couple to a perfectly centered electron will couple more strongly to the electrons as their number is increased so that they occupy a larger volume. From 2006 to 2008 our understanding of the cavity improved when we became aware of, and were able to measure, a small displacement of the electrostatic center of the trap (where the electron resides), and the center for the cavity radiation modes.

So far we have used the calculable cylindrical trap geometry to know which radiation modes can couple to an electron near the center of the

184   *G. Gabrielse*

trap, and we have recognized these modes in measured cavity spectra by comparing their measured frequencies to what is calculated for a perfect cavity. Next we use the measured radiation mode frequencies and quality factors as input to a calculation of the cavity shift of the electron cyclotron frequency as a function of the electron cyclotron frequency (Fig. 5.8d).

A calculation of the shifts [37, 40] must carefully distinguish and remove the electron self-energy from the electron-cavity interaction. The uncertainty in the measured inputs gives a cavity shift uncertainty (Fig. 5.8e) that is small between the resonance frequencies of modes that couple strongly to a centered electron, and then increases strongly closer to the resonant frequencies of these modes. The diamonds at the top of the figure show how, in our four measurements of $g/2$, we avoid the electron cyclotron frequencies for which the uncertainty is the largest. Fig. 5.10 shows the good agreement attained between the four measurements when the cavity shifts are applied.
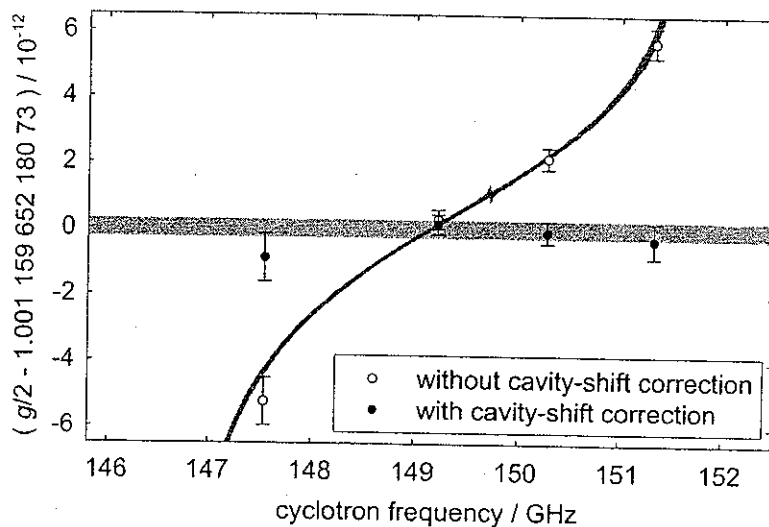

Fig. 5.10. Four measurements of $g/2$ without (open) and with (filled) cavity-shift corrections. The light gray uncertainty band shows the average of the corrected data. The dark gray band indicates the expected location of the uncorrected data given our result in Eq. (5.23) and including only the cavity shift uncertainty.

Table 5.2. Measurements and shifts with uncertainties multiplied by 10^{12}. The cavity-shifted "$g/2$ raw" and corrected "$g/2$" are offset from our result in Eq. (5.23).

f_c	147.5 GHz	149.2 GHz	150.3 GHz	151.3 GHz
$g/2$ raw	-5.24 (0.39)	0.31 (0.17)	2.17 (0.17)	5.70 (0.24)
Cav. shift	4.36 (0.13)	-0.16 (0.06)	-2.25 (0.07)	-6.02 (0.28)
Lineshape				
correlated	(0.24)	(0.24)	(0.24)	(0.24)
uncorrelated	(0.56)	(0.00)	(0.15)	(0.30)
$g/2$	-0.88 (0.73)	0.15 (0.30)	-0.08 (0.34)	-0.32 (0.53)

5.5. Results and Applications

5.5.1. *Most accurate electron $g/2$*

The measured values, shifts, and uncertainties for the four separate measurements of $g/2$ are in Table 5.2. The uncertainties are lower for measurements with smaller cavity shifts and smaller linewidths, as might be expected. Uncertainties for variations of the power of the $\bar{\nu}_a$ and $\bar{f}_c$ drives are estimated to be too small to show up in the table. A weighted average of the four measurements, with uncorrelated and correlated errors combined appropriately, gives the electron magnetic moment in Bohr magnetons,

$$g/2 = 1.001\,159\,652\,180\,73\,(28) \qquad [0.28\text{ ppt}]. \qquad (5.23)$$

The uncertainty is 2.7 and 15 times smaller than the 2006 and 1987 measurements, and 2300 times smaller than has been achieved for the heavier muon lepton [41].

5.5.2. *Most accurate determination of α*

The new measurement determines the fine structure constant, $\alpha = e^2/(4\pi\epsilon_0\hbar c)$, much more accurately than does any other method. The fine structure constant is the fundamental measure of the strength of the electromagnetic interaction in the low energy limit, and it is also a crucial ingredient of our system of fundamental constants [42]. A full discussion of α, its importance, the quantum electrodynamics theory used to determine it from the measured $g/2$, and alternative methods to determine α is in Chapter 6. Only the bare essentials of what is needed to determine α from $g/2$ are summarized here.

G. Gabrielse

Measurements of the Electron Magnetic Moment
Chapter 5 in "Lepton Moments"

Edited by Roberts and Marciano
(World Scientific, Singapore, 2010)

186

G. Gabrielse

The Standard Model relates g and α by

$$\frac{g}{2} = 1 + C_2 \left(\frac{\alpha}{\pi}\right) + C_4 \left(\frac{\alpha}{\pi}\right)^2 + C_6 \left(\frac{\alpha}{\pi}\right)^3 + C_8 \left(\frac{\alpha}{\pi}\right)^4$$
$$+ C_{10} \left(\frac{\alpha}{\pi}\right)^5 + ... + a_{\text{hadronic}} + a_{\text{weak}}, \tag{5.24}$$

with the asymptotic series and the values of the C_k coming from QED. Very small hadronic and weak contributions are included, along with the assumption that there is no significant modification from electron substructure or other physics beyond the Standard Model.

QED calculations (summarized more extensively in Chapter 6) give the constants C_k,

$$C_2 = \quad 0.500\ 000\ 000\ 000\ 00 \text{ (exact)} \tag{5.25}$$
$$C_4 = -\ 0.328\ 478\ 444\ 002\ 90\ (60) \tag{5.26}$$
$$C_6 = \quad 1.181\ 234\ 016\ 827\ (19) \tag{5.27}$$
$$C_8 = -\ 1.914\ 4\ (35) \tag{5.28}$$
$$C_{10} = \quad 0.0\ (4.6). \tag{5.29}$$

The QED theory for C_2 [43], C_4 [11, 13, 44], and C_6 [47] is exact, with no uncertainty, except for an essentially negligible uncertainty in C_4 and C_6 that comes from a weak functional dependence upon the lepton mass ratios, m_μ/m_e and m_τ/m_e. Numerical QED calculations [48] give the value and uncertainty for C_8. The hadronic anomaly a_{hadronic}, calculated within the context of the Standard Model,

$$a_e^{\text{hadronic}} = 1.682(20) \times 10^{-12}, \tag{5.30}$$

contributes at the level of several times the current experimental uncertainty, but the calculation uncertainty in the hadronic anomaly is not important [38, 42]. See Chapters 8 and 9 for further details. The weak anomaly is completely negligible.

The most accurately determined fine structure constant is given by

$$\alpha^{-1} = 137.035\ 999\ 084\ (33)\ (39)\quad [0.24\ \text{ppb}]\ [0.28\ \text{ppb}],$$
$$= 137.035\ 999\ 084\ (51)\qquad [0.37\ \text{ppb}]. \tag{5.31}$$

The first line shows experimental (first) and theoretical (second) uncertainties that are nearly the same. The theory uncertainty contribution to α is divided as (12) and (37) for C_8 and C_{10}. It should decrease when a calculation underway [48] replaces the crude estimate $C_{10} = 0.0\,(4.6)$ [42, 50]. The α^{-1} of Eq. (5.31) will then shift by $2\alpha^3\pi^{-4}C_{10}$, which is $8.0\,C_{10} \times 10^{-9}$. A change Δ_8 in the calculated C_8 would add $2\alpha^2\pi^{-3}\Delta_8$.

The total 0.37 ppb uncertainty in α is 12 and 21 times smaller than for the next most precise independent methods (Fig. 5.11). These so-called atom recoil methods (see Chapter 6) utilize measurements of the Rydberg constant [17, 51], transition frequencies [21, 53], mass ratios [19, 55], and either a Rb [54] or Cs [57] recoil velocity measured in an atom interferometer.
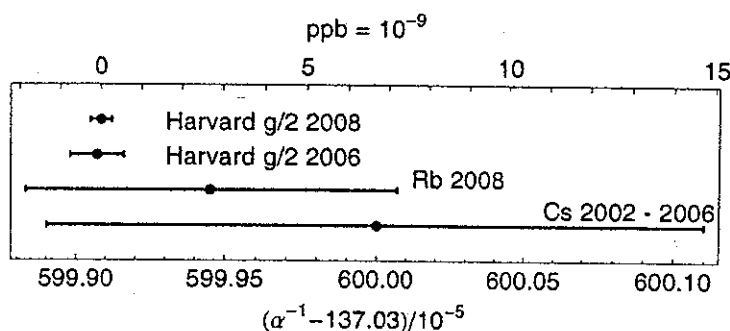

Fig. 5.11. The most accurate determinations of α are determined from the measured electron $g/2$. These are compared to the best independently measured values.

5.5.3. *Testing the standard model and QED*

The dimensionless electron magnetic moment g that is measured can be compared to the $g(\alpha)$ that is predicted by the Standard Model of particle physics. The input needed to calculate $g(\alpha)$ is the measured fine structure constant α (that is determined without the use of the electron magnetic moment). The most accurately measured and calculated values of $g/2$ are currently given by

$$g/2 = 1.001\ 159\ 652\ 180\ 73\ \ (28)\ [0.28\ \text{ppt}], \qquad (5.32)$$
$$g(\alpha)/2 = 1.001\ 159\ 652\ 177\ 60\ (520)\ [5.2\ \ \text{ppt}]. \qquad (5.33)$$

The measurement is our one-electron quantum cyclotron measurement [6]. The calculated value $g(\alpha)/2$ comes from using the Rb value of $\alpha(\text{Rb08})$ in Eq. (5.24). The large uncertainty in this "calculated" value actually comes from the large uncertainty in the Rb α; the theoretical uncertainty is believed to be much smaller, comparable to the measurement uncertainty for $g/2$. The Standard Model prediction is thus tested and verified to about 5 ppt. The much smaller 0.3 ppt uncertainty in the measured $g/2$, along with the comparable uncertainty in the QED calculation, would allow a much better test of QED.
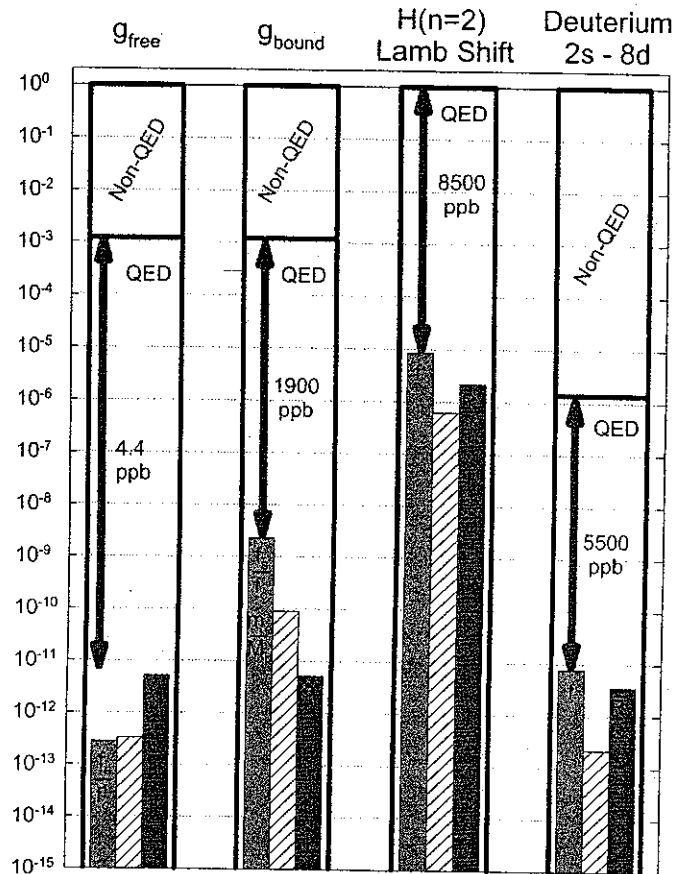
188   *G. Gabrielse*

Fig. 5.12. Comparisons of precise tests of QED. The arrows represent the fractional accuracy to which the QED contribution to the measured g values and frequencies that are measured.

About 1 part per thousand of the electron $g/2$ comes from the unavoidable interaction of the electron with the virtual particles of "empty space", as described by quantum electrodynamics (QED) and represented in Fig. 5.12. Where testing QED is the primary focus, measured and calculated values of the so-called anomalous magnetic moment of the electron (defined by $a = g/2 - 1$ so that the Dirac contribution is subtracted out) are often compared. The measured and calculated values of a that correspond to the $g/2$ values above are

$$a = 0.001\ 159\ 652\ 180\ 73\ (\ 28)\ [0.24\ \text{ppb}], \qquad (5.34)$$

$$a(\alpha) = 0.001\ 159\ 652\ 177\ 60\ (520)\ [4.4\ \text{ppb}]. \qquad (5.35)$$

At the one standard deviation level, the difference of the measured and

G. Gabrielse | Measurements of the Electron Magnetic Moment
Chapter 5 in "Lepton Moments" | Edited by Roberts and Marciano
(World Scientific, Singapore, 2010)

calculated values is

$$\delta a = a - a(\alpha) \tag{5.36}$$

$$= g/2 - g(\alpha)/2 \tag{5.37}$$

$$= 3.1(5.2) \times 10^{-12}. \tag{5.38}$$

The possible difference between the measurement and calculation is thus bounded by

$$|\delta a| < 8.3 \times 10^{-12}, \tag{5.39}$$

at the one standard deviation level, with this bound arising almost entirely from the uncertainty in the measurement of α from Rb.

Some of the most precise tests of bound-state QED are compared in Fig. 5.12 with the electron $g/2$. The QED test based upon the measurements [56] and calculation [58] of $g/2$ for an electron bound in an ion provides a test of the QED contribution to the electron magnetic moment at the 4.4 ppb level. Bound electron $g/2$ measurements test QED less precisely. In fact, the calculated value of the bound g values depends upon the mass of the electron strongly enough that this measurement is now being used to determine the electron mass in amu, much as we determine α from our measurements of the magnetic moment of the free electron. The n=2 Lamb shift in hydrogen is essentially entirely due to QED. However, the measurements are much less precise so that QED is again tested less precisely.

The last example in the figure is a QED test based upon a number of measurements of hydrogen and deuterium transition frequencies – the QED contribution to which are typically at the ppm level. Theoretical calculations that depend upon the Rydberg constant, the fine structure constant, the ratio of the electron and proton masses and the size of the nucleus are fit to a number of accurately measured transition frequencies for hydrogen and deuterium. The fit determines values for the mentioned constants. The QED test comes from removing one of the measured lines from the fit, and using the best fit to predict the value of the transition frequency that was omitted. This process tests the Standard Model prediction at a comparable precision to that provided using the magnetic moment of the electron. However, it tests the size of the QED contribution to a much lower fractional precision.

The QED tests described so far test QED predictions to the highest precision and the highest order in α. There are many other tests of QED with a much lower precision. Although these tests are outside of the scope

of this work it is worth mentioning that it is interesting to probe QED in other ways. For example, it seems interesting to test QED for systems whose binding energy is very large, even comparable to the electron rest mass energy as can be done in high Z systems. Another example is probing the QED of positronium, the bound state of an electron and a positron, insofar as annihilation and exchange effects are quite different than what must be calculated for normal atoms.

5.5.4. *Probe for electron substructure*

Comparing experiment and theory probes for possible electron substructure at an energy scale one might only expect from a large accelerator. An electron whose constituents would have mass $m^* \gg m$ has a natural size scale, $R = \hbar/(m^* c)$. The simplest analysis of the resulting magnetic moment [59] gives $\delta a \sim m/m^*$, suggesting that $m^* > 61{,}000$ TeV/c^2 and $R < 3 \times 10^{-24}$ m. This would be an incredible limit, since the largest $e^+ e^-$ collider (LEP) probes for a contact interaction at an $E = 10.3$ TeV [60], with $R < (\hbar c)/E = 2 \times 10^{-20}$ m.

However, the simplest argument also implies that the first-order contribution to the electron self-energy goes as m^* [59]. Without heroic fine tuning (e.g. the bare mass canceling this contribution to produce the small electron mass) some internal symmetry of the electron model must suppress both mass and moment. For example, a chirally invariant model [59], leads to $\delta a \sim (m/m^*)^2$. In this case, $m^* > 177$ GeV/c^2 and $R < 1 \times 10^{-18}$ m. These limits seem remarkable for an experiment carried out at 100 mK, although they do not compete with LEP. If this test was limited only by the experimental uncertainty in a then we could set a limit $m^* > 1$ GeV.

5.5.5. *Comparison to the muon g/2*

The electron $g/2$ is measured about 2300 times more accurately than is $g/2$ for its heavier muon sibling [7, 41]. Because the electron is stable there is time to isolate one electron, cool it so that it occupies a very small volume within a magnetic field, and to resolve the quantum structure in its cyclotron and spin motions. The short-lived muon must be studied before it decays in a very small fraction of a second, during which time it orbits in a very large orbit over which the same magnetic field homogeneity realized with a nearly motionless electron cannot be maintained.

Why then measure the muon $g/2$? The compelling reason is that the muon $g/2$ is expected to be more sensitive to physics beyond the Standard

Model by about a factor of 4×10^4, which is the square of the ratio of the muon to the electron mass. In terms of Eq. (5.2) this means that a_{new} is expected to be bigger for the muon than for the electron by this large factor, making the muon a more attractive probe for New Physics.

Unfortunately, the other Standard Model contribution, $a_{\text{hadronic}} + a_{\text{weak}}$, is also bigger by approximately the same large factor, rather than being essentially negligible as in the electron case. Correctly calculating these terms is a significant challenge to detecting New Physics. These large terms, and the much lower measurement precision, also make the muon an unattractive candidate (compared to the electron) for determining the fine structure constant and for testing QED.

The measured electron $g/2$ makes two contributions to using the muon system for probing for physics beyond the Standard Model. Both relate to determining the muon QED anomaly $a_{\text{QED}}(\alpha)$

(1) The electron measurement of $g/2$ makes possible the most accurate determination of the fine structure constant (discussed in the previous section and in Chapter 6) as is needed to calculate $a_{\text{QED}}(\alpha)$.

(2) The electron measurement of $g/2$ and an independently measured value of α test QED calculations of the very similar $a_{\text{QED}}(\alpha)$ terms in the electron system.

The QED contribution must be accurately subtracted from the measured muon $g - 2$ if the much smaller possible contribution from New Physics is to be observed.

5.6. Prospects and Conclusion

In conclusion, our 2008 measurement of the electron $g/2$ is 15 times more accurate than the 1987 measurement that provided $g/2$ and α for nearly 20 years, and 2.7 times more accurate than our 2006 measurement that superseded it. Achieving the reported electron $g/2$ uncertainty with a positron seems feasible, to make the most stringent lepton CPT test.

With QED and the assumption of no New Physics beyond the Standard Model of particle physics, the new measurement determines α 12 times more accurately than any independent method. The measured $g/2$ makes it possible to test QED and probe for electron size. In fact, the sensitivity of all of these applications would immediately be improved by the factor of 12 if a more accurate independent measurement of α, at our level of precision, is realized.

G. Gabrielse

Several experimental items warrant further study. First is the broadening of the expected lineshapes which limits the splitting of the resonance lines. Second, the variation in axial temperatures in the observed resonance lineshapes is not understood, and a larger uncertainty comes from the wider lineshapes. Third, cavity sideband cooling could cool the axial motion to near its quantum ground state for a more controlled measurement. Fourth, a new apparatus should be much less sensitive to vibration and other variations in the laboratory environment. A more accurate measurement of the electron $g/2$ is the expected result.

Acknowledgments

References

[1] B. Lautrup and H. Zinkernagel, *Stud. Hist. Phil. Mod. Phys.* **30**, 85 – 110, (1999).

[2] A. Rich and J. C. Wesley, *Rev. Mod. Phys.* **44**, 250, (1972).

[3] R. S. Van Dyck Jr. , P. B. Schwinberg, and H. G. Dehmelt, *The Electron*, pp. 239–293. Kluwer Academic Publishers, Netherlands, (1991).

[4] R. S. Van Dyck, Jr., P. B. Schwinberg, and H. G. Dehmelt, *Phys. Rev. Lett.* **59**, 26–29, (1987).

[5] B. Odom, D. Hanneke, B. D'Urso, and G. Gabrielse, *Phys. Rev. Lett.* **97**, 030801, (2006).

[6] D. Hanneke, S. Fogwell, and G. Gabrielse, *Phys. Rev. Lett.* **100**, 120801, (2008).

[7] L. S. Brown and G. Gabrielse, *Rev. Mod. Phys.* **58**, 233–311, (1986).

[8] L. S. Brown and G. Gabrielse, *Phys. Rev. A.* **25**, 2423–2425, (1982).

[9] G. Gabrielse and F. C. MacKintosh, *Intl. J. of Mass Spec. and Ion Proc.* **57**, 1–17, (1984).

[10] J. N. Tan and G. Gabrielse, *Appl. Phys. Lett.* **55**, 2144–2146, (1989).

[11] G. Gabrielse, *Phys. Rev. A.* **27**, 2277–2290, (1983).

[12] L. S. Brown, G. Gabrielse, J. N. Tan, and K. C. D. Chan, *Phys. Rev. A.* **37**, 4163–4171, (1988).

[13] J. D. Jackson, *Classical Electrodynamics, 2nd Edition.* (John Wiley and Sons, Inc., New York, 1975).

G. Gabrielse

Measurements of the Electron Magnetic Moment
Chapter 5 in "Lepton Moments"

Edited by Roberts and Marciano
(World Scientific, Singapore, 2010)

Measurements of the Electron Magnetic Moment   193

[14] J. Tan and G. Gabrielse, *Phys. Rev. Lett.* **67**, 3090–3093, (1991).

[15] J. N. Tan and G. Gabrielse, *Phys. Rev. A.* **48**, 3105–3122, (1993).

[16] G. Gabrielse, J. N. Tan, and L. S. Brown, *Cavity Shifts of Measured Electron Magnetic Moments*, In (ed.) T. Kinoshita, *Quantum Electrodynamics*, pp. 389–418. World Scientific, Singapore, (1990).

[17] G. Gabrielse, X. Fei, L. A. Orozco, R. L. Tjoelker, J. Haas, H. Kalinowsky, T. A. Trainor, and W. Kells, *Phys. Rev. Lett.* **65**, 1317–1320, (1990).

[18] G. Gabrielse and J. Tan, *J. Appl. Phys.* **63**, 5143–5148, (1988).

[19] G. Gabrielse, J. N. Tan, L. A. Orozco, S. L. Rolston, C. H. Tseng, and R. L. Tjoelker, *J. Mag. Res.* **91**, 564–572, (1991).

[20] E. S. Meyer, I. F. Silvera, and B. L. Brandt, *Rev. Sci. Instrum.* **60**, 2964–2968, (1989).

[21] D. F. Phillips. *A Precision Comparison of the $\bar{p} - p$ Charge-to-Mass Ratios*. Ph.D. thesis, Harvard University, (1996).

[22] R. S. Van Dyck, Jr., D. L. Farnham, S. L. Zafonte, and P. B. Schwinberg, *Rev. Sci. Instrum.* **70**, 1665–1671, (1999).

[23] B. Odom. *Fully Quantum Measurement of the Electron Magnetic Moment*. Ph.D. thesis, Harvard University, (2004).

[24] G. Gabrielse and H. Dehmelt, *Phys. Rev. Lett.* **55**, 67–70, (1985).

[25] S. Peil and G. Gabrielse, *Phys. Rev. Lett.* **83**, 1287–1290, (1999).

[26] K. S. Thorne, R. W. P. Drever, and C. M. Caves, *Phys. Rev. Lett.* **40**(11), 667–670, (1978).

[27] V. B. Braginsky and F. Y. Khalili, *Rev. Mod. Phys.* **68**(1-11), 1, (1996).

[28] B. D'Urso. *Cooling and Self-Excitation of a One-Electron Oscillator*. Ph.D. thesis, Harvard Univ., (2003).

[29] R. Van Dyck, Jr., P. Ekstrom, and H. Dehmelt, *Nature.* **262**, 776, (1976).

[30] B. D'Urso, B. Odom, and G. Gabrielse, *Phys. Rev. Lett.* **90**(4), 043001, (2003).

[31] B. D'Urso, R. Van Handel, B. Odom, D. Hanneke, and G. Gabrielse, *Phys. Rev. Lett.* **94**, 113002, (2005).

[32] D. J. Wineland and H. G. Dehmelt, *J. Appl. Phys.* **46**, 919–930, (1975).

[33] R. Kubo, *Rep. Prog. Phys.* **29**(1), 255–284, (1966).

[34] E. M. Purcell, *Phys. Rev.* **69**, 681, (1946).

[35] D. Kleppner, *Phys. Rev. Lett.* **47**, 233, (1981).

[36] F. L. Palmer, *Phys. Rev. A.* **47**, 2610, (1993).

[37] L. S. Brown, *Ann. Phys. (N.Y.).* **159**, 62–98, (1985).

[38] D. G. Boulware, L. S. Brown, and T. Lee, *Phys. Rev. D.* **32**, 729–735, (1985).

[39] G. Gabrielse and J. N. Tan, *One Electron in a Cavity*, In ed. P. Berman, *Cavity Quantum Electrodynamics*, pp. 267–299. Academic Press, New York, (1994).

[40] L. S. Brown, *Phys. Rev. Lett.* **52**, 2013–2015, (1984).

[41] G. W. Bennett and *et al.*, *Phys. Rev. D.* **73**, 072003, (2006).

[42] P. J. Mohr and B. N. Taylor, *Rev. Mod. Phys.* **77**, 1 – 107, (2005).

[43] J. Schwinger, *Phys. Rev.* **73**, 416L, (1948).

[44] A. Petermann, *Helv. Phys. Acta.* **30**, 407, (1957).

[45] C. M. Sommerfield, *Phys. Rev.* **107**, 328, (1957).

194 *G. Gabrielse*

[46] C. M. Sommerfield, *Ann. Phys. (N.Y.).* **5**, 26, (1958).

[47] S. Laporta and E. Remiddi, *Phys. Lett. B.* **379**, 283, (1996).

[48] T. Aoyama, M. Hayakawa, T. Kinoshita, and M. Nio, *Phys. Rev. Lett.* **99**, 110406, (2007).

[49] A. Czarnecki, B. Krause, and W. J. Marciano, *Phys. Rev. Lett.* **76**, 3267–3270, (1996).

[50] G. Gabrielse, D. Hanneke, T. Kinoshita, M. Nio, and B. Odom, *Phys. Rev. Lett.* **97**, 030802, (2006). *ibid.* **99**, 039902 (2007).

[51] T. Udem, A. Huber, B. Gross, J. Reichert, M. Prevedelli, M. Weitz, and T. W. Hänsch, *Phys. Rev. Lett.* **79**, 2646–2649, (1997).

[52] C. Schwob, L. Jozefowski, B. de Beauvoir, L. Hilico, F. Nez, L. Julien, F. Biraben, O. Acef, J. J. Zondy, and A. Clairon, *Phys. Rev. Lett.* **82**, 4960–4963, (1999).

[53] V. Gerginov, K. Calkins, C. E. Tanner, J. J. McFerran, S. Diddams, A. Bartels, and L. Hollberg, *Phys. Rev. A.* **73**, 032504, (2006).

[54] M. Cadoret, E. de Mirandes, P. Cladé, S. Guellati-Hkélifa, C. Schwob, F. Nez, L. Julien, and F. Biraben, *Phys. Rev. Lett.* **101**, 230801, (2008).

[55] M. P. Bradley, J. V. Porto, S. Rainville, J. K. Thompson, and D. E. Pritchard, *Phys. Rev. Lett.* **83**, 4510–4513, (1999).

[56] G. Werth, J. Alonso, T. Beier, K. Blaum, S. Djekic, H. Häffner, N. Hermanspahn, W. Quint, S. Stahl, J. Verdú, T. Valenzuela, and M. Vogel, *Int. J. Mass Spectrom.* **251**, 152, (2006).

[57] A. Wicht, J. M. Hensley, E. Sarajlic, and S. Chu, *Phys. Scr.* **T102**, 82–88, (2002).

[58] K. Pachucki, A. Czarnecki, U. Jentschura, and V. A. Yerokhin, *Phys. Rev. A.* **72**, 022108, (2005).

[59] S. J. Brodsky and S. D. Drell, *Phys. Rev. D.* **22**, 2236–2243, (1980).

[60] D. Bourilkov, *Phys. Rev. D.* **64**, 071701R, (2001).